

Quantitative Mineral Mapping of Drill Core Surfaces I: A Method for μ XRF Mineral Calculation and Mapping of Hydrothermally Altered, Fine-Grained Sedimentary Rocks from a Carlin-Type Gold Deposit

Rocky D. Barker,^{1,†} Shaun L.L. Barker,^{2,*} Siobhan A. Wilson,³ and Elizabeth D. Stock⁴

¹*School of Science, University of Waikato, Private Bag 3105, Hamilton, New Zealand 3240*

²*CODES ARC Centre of Excellence in Ore Deposits, University of Tasmania, Private Bag 126, Hobart, Tasmania, Australia 7001*

³*Department of Earth and Atmospheric Sciences, University of Alberta, Edmonton, Alberta, Canada T6G 2E3*

⁴*Barrick Gold Exploration Inc., 1655 Mountain City Hwy, Elko, Nevada 89801*

Abstract

Mineral distributions can be determined in drill core samples from a Carlin-type gold deposit, using micro-X-ray fluorescence (μ XRF) raster data. Micro-XRF data were collected using a Bruker Tornado μ XRF scanner on split drill core samples ($\sim 25 \times 8$ cm) with data collected at a spatial resolution of $\sim 100 \mu\text{m}$. Bruker AMICS software was used to identify mineral species from μ XRF raster data, which revealed that many individual sample spots were mineral mixtures due to the fine-grained nature of the samples. In order to estimate the mineral abundances in each pixel, we used a linear programming (LP) approach on quantified μ XRF data. Quantification of μ XRF spectra was completed using a fundamental parameters (FP) standardless approach. Results of the FP method compared to standardized wavelength dispersive spectrometry (WDS)-XRF of the same samples showed that the FP method for quantification of μ XRF spectra was precise (R^2 values of 0.98–0.97) although the FP method gave a slight overestimate of Fe and K and an underestimate of Mg abundance. Accuracy of the quantified μ XRF chemistry results was further improved by using the WDS-XRF data as a calibration correction before calculating mineralogy using LP. The LP mineral abundance predictions were compared to Rietveld refinement results using X-ray diffraction (XRD) patterns collected from powders of the same drill core samples. The root mean square error (RMSE) for LP-predicted mineralogy compared to quantitative XRD results ranges from 0.91 to 7.15% for quartz, potassium feldspar, pyrite, kaolinite, calcite, dolomite, and illite.

The approaches outlined here demonstrates that μ XRF maps can be used to determine mineralogy, mineral abundances, and mineralogical textures not visible with the naked eye from fine-grained sedimentary rocks associated with Carlin-type Au deposits. This approach is transferable to any ore deposit, but particularly useful in sedimentary-hosted ore deposits where ore and gangue minerals are often fine grained and difficult to distinguish in hand specimen.

Introduction

Understanding the distribution of minerals within ore deposits is important to determine the mineralization and alteration paragenesis, recognize the distribution and type of ore minerals, and understand how mineralogy influences ore processing (e.g., silicate mineral abundances; Johnson et al., 2019). Large-scale mineralogical studies have shown to be of great value in recent years with the advent of mineral mapping technologies, such as infrared spectrographic imaging and quantitative scanning electron microscopy (qSEM; Gottlieb, 2008). Understanding mineral distributions in rocks is of particular value to the mineral industry, where ascertaining the distribution of

mineral species in a deposit could be beneficial to defining mineral resources, or more efficiently processing ore. Micro-X-ray fluorescence (μ XRF) scanning is a relatively new analytical tool that allows chemical mapping of rock samples at a very fine scale ($< 100 \mu\text{m}$), yet on sample sizes that lie between traditional SEM thin-section observations ($< \sim 1$ mm) and the core-scale observations made during logging and assay chemistry (~ 1 mm to m). Examples of applications of geochemical analyses using μ XRF include studies of volcanogenic massive sulfides (Genna et al., 2011), shale-hosted uranium (Xu et al., 2015), greenstone-hosted Cu-Co-Au (Fox et al., 2019), and environmental sciences (Croudace and Rothwell, 2015; Flude et al., 2017). In each of these studies, μ XRF is used to visualize and, in some cases, quantify (Flude et al., 2017) the distribution of elements over the surface of mineral and rock samples, which in turn reveals textures and patterns that cannot be observed in hand

[†]Corresponding author: e-mail, rdb28@students.waikato.ac.nz

*Present address: Mineral Deposit Research Unit, Department of Earth, Ocean and Atmospheric Sciences, University of British Columbia, Vancouver, BC, Canada.

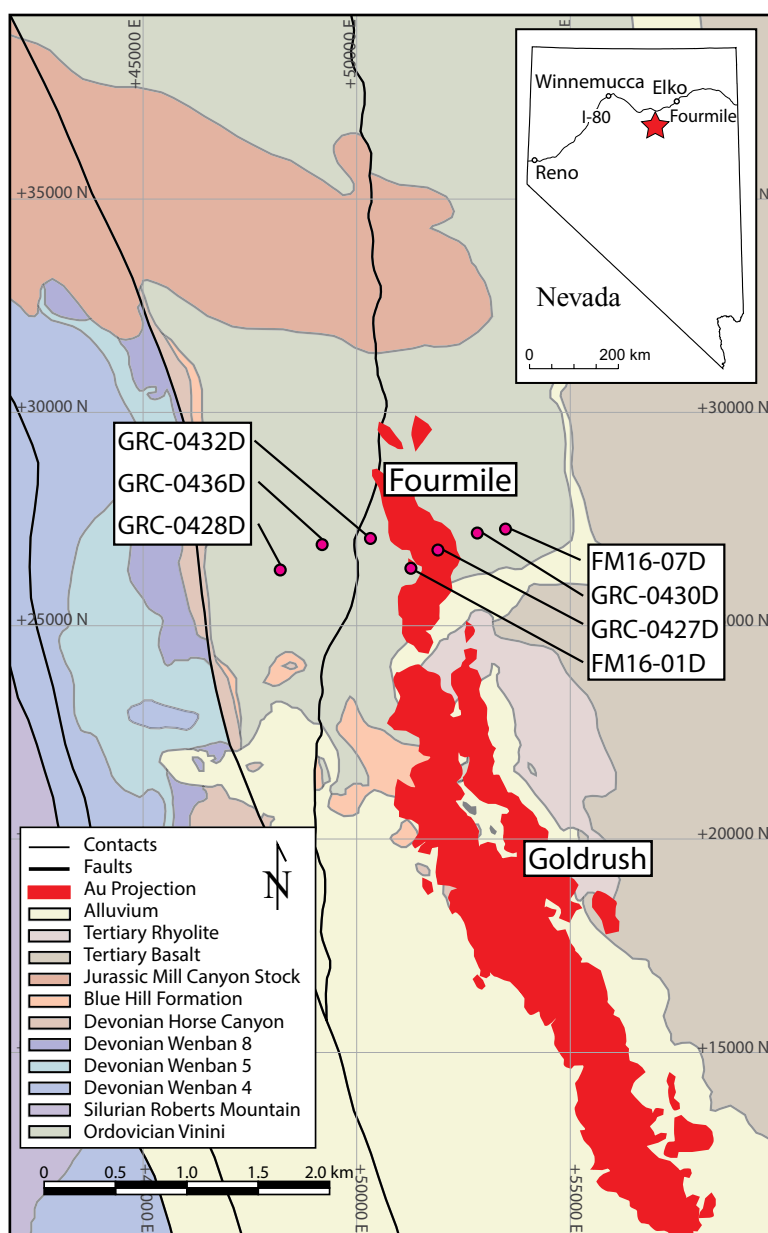


Fig. 1. Regional geologic map of the Goldrush-Fourmile district from Barrick Gold Exploration Inc. unpublished results with locations of drill holes, which sourced the samples for this study.

samples. These chemical data, as shown here in this research, can also be interpreted in terms of mineral species.

The rocks analyzed in this study were selected from seven drill holes arranged in a transect (Fig. 1, Table 1) across hydrothermally altered and unaltered Paleozoic passive margin carbonate, carbonaceous shales, and siliciclastic rocks (Stewart, 1980) of the Fourmile Carlin-type Au discovery in Nevada. Mineralogy of Carlin-type deposits can be difficult to identify in hand specimen or thin section due to their fine-grained nature (Muntean, 2018). It is difficult to use shortwave infrared spectroscopy to identify minerals in the rocks which host Carlin-type gold deposits, because of the fine-grained samples and the lack of reflectance (Ahmed et al., 2010; Barker, 2017). In this study we show that μ XRF can be used to accurately quantify elemental abundances via a fundamental parameters

(FP) method by comparing FP results of rock samples with traditional whole-rock geochemistry analyses (WDS-XRF and 4-acid digest methods). In addition, quantified μ XRF chemistry results can be further improved by calibrating FP results from rock powders with WDS-XRF results collected from the same rock samples. Finally, we demonstrate two methods for mineral identification and quantification using μ XRF raster maps. The first method is a demonstration of the utility of the Bruker AMICS software (Bruker, 2018a) for mineral identification from μ XRF spectra through a combination of XRF spectra library matching and clustering algorithms. For the second method we show that μ XRF spectra can be accurately quantified and used to predict and map the quantitative mineral abundance across samples using a linear programming (LP) approach.

Table 1. List of Samples Used for XRF-WDS, Whole-Rock Geochemistry, QXRD, and μ XRF (chemical maps and quantitative extractions) Analyses with Broad Description of Lithology and Alteration Type

Drill hole	Sample	Depth (m)	μ XRF (map)	μ XRF (quant)	XRF-WDS	Whole rock	QXRD	MLA	Rock description
FM16-01D	M180059	535.38		1	1	x	x		Silicified, decalcified, and sulfidized argillitic carbonaceous mudstone
FM16-01D	M180062	609.57	x	1	1	x	x	x	Silicified and brecciated limey carbonaceous mudstone with illite enrichment
FM16-01D	M180065	745.91		2	2	x	x		Pervasively sulfidized and argillized limey mudstone fault rock
FM16-01D	M180069	863.44		2	2	x	x		Limestone with minor silicification and argillization
FM16-01D	M180074	1071.59		2	2	x	x		Sulfidized and argillized muddy limestone
FM16-07D	M180077	706.53		2	2	x	x		Metacarbonate breccia with silicified clasts
FM16-07D	M180080	823.48	x	1	1	x	x		Limey mudstone with silica replacement front
FM16-07D	M180083	906.48		1	1	x	x		Dolomitic metacarbonate
FM16-07D	M180088	1118.07		1	1	x	x		Base metal vein-bearing marl with minor silicification
GRC-0427D	M180093	685.69		2	2	x	x		Metacarbonate with pinstripe pyrite and minor silicification
GRC-0427D	M180095	715.11	x	2	2	x	x	x	Pervasively argillized limey mudstone with minor sulfidation and silicification
GRC-0427D	M180097	726.20		1	1	x			Carbonaceous limey mudstone breccia
GRC-0427D	M180098	736.71		1	1	x	x		Pervasively dolomitized limey mudstone
GRC-0427D	M180099	764.50		1	1	x	x		Muddy limestone with minor silicification and argillization
GRC-0427D	M180101	823.05		1	1	x			Muddy limestone with minor silicification and argillization
GRC-0427D	M180102	877.00		1	1	x	x		Muddy limestone with minor silicification and argillization
GRC-0427D	M180104	925.07		1	1	x	x		Mineralized limey mudstone breccia with pervasive silicification and sulfidation
GRC-0436D	M180109	520.93		2	2	x	x		Argillitic carbonaceous mudstone
GRC-0436D	M180118	765.20		2	2	x	x		Muddy limestone with minor silicification and argillization
GRC-0432D	M180121	200.62		1	1	x	x		Weathered carbonaceous limey mudstone with minor argillization and silicification
GRC-0432D	M180123	296.27		1	1	x			Carbonaceous limey mudstone
GRC-0432D	M180127	420.29		1	1	x			Limestone
GRC-0432D	M180130	555.04	x	2	2	x	x	x	Limey mudstone with silica replacement front and sulfidation
GRC-0432D	M180136	814.09		1	1	x			Muddy limestone
GRC-0428D	M180145	763.86		1	1	x	x		Metacarbonate with minor silicification and sulfidation
GRC-0430D	M180152	654.50		2	2	x	x		Marble
GRC-0430D	M180157	855.42		3	3	x	x		Metacarbonate
GRC-0430D	M180161	1039.31		1	1	x	x		Carbonaceous limey mudstone

Numbers in the μ XRF [quant] and XRF-WDS columns represent the number of subsamples taken from different areas of the core sample; QXRD = quantitative X-ray diffraction, WDS = wavelength dispersive spectrometry, μ XRF = micro-X-ray fluorescence

Methodology

Micro-XRF fundamental parameters standardless quantification

There are two general types of quantification methods for use with X-ray fluorescence spectra: standard-based (empirical) and standardless quantification procedures (such as fundamental parameters). Current methods for quantification of elemental abundances from XRF data use a fundamental parameters (FP) approach adapted from the Sherman equation (Sherman, 1955) to calculate concentrations from peak intensities (Thomsen, 2007; Flude et al., 2017). These methods are referred to as fundamental parameters methods, a name that comes from the set of parameters which describe X-ray interactions with atoms that are used to predict chemical proportions from X-ray peak intensities (Elam et al., 2004).

Micro-XRF data are collected from whole-rock samples rather than powders, producing two-dimensional arrays (maps) of XRF spectra that capture the spatial variation of elemental composition and mineralogy. Standardless FP quantification is considered to be the best option for quantification of μ XRF data due to the large compositional variations found within small areas of most rock samples, which would otherwise require that a large set of reference materials be used in

a standard-based quantification method (Kamngießer, 2003; Flude et al., 2017). This is further complicated by the potential difficulty in selecting a suitable reference material, which is homogeneous at the spatial scale of the μ XRF beam (~20–100 μ m). Given that the results of FP quantification are comparable to the standard-based method (Wegrzynek et al., 1998; Tagle and Reinhardt, 2016; Flude et al., 2017), it is difficult to justify using a standard-based approach for μ XRF analyses.

Comparison of geochemical results from a standard-based quantification method and FP quantification shows that there is general agreement between the two methods (Wegrzynek et al., 1998). In the case of complicated samples (complex matrix with a high number of low Z elements) the FP algorithm performed slightly better at quantification. In a report by Tagle and Reinhardt (2016), they show that the FP quantification method available in the Bruker M4 software (Bruker, 2018b) performs well at quantifying homogeneous stainless-steel certified standards. Flude et al. (2017), however, found that the accuracy of the M4 FP method was diminished in some heterogeneous silicate material, but could be greatly improved using a hybrid standard-based/FP method, where a standard is analyzed and a type calibration was used to correct the FP results.

Micro-XRF geochemical maps for this study were produced on a Bruker Tornado μ XRF scanner (Bruker, 2018c),

using a 100- μm step size and 25- μm spot size with standard conditions of analyses at 10 ms/pixel, two frame counts, and 50-kV acceleration voltage at the AuTec Laboratory in Vancouver, Canada. Quantitative chemical results were derived using the Bruker M4 (Bruker, 2018b) QMap fundamental parameters standardless quantification tool (Tagle and Reinhardt, 2016). The Bruker FP algorithm iteratively solves a variation of the Sherman equation, while automatically correcting for detector pile up and escape peaks to produce chemical concentrations using X-ray peak intensities. The FP algorithm uses a database of atomic fundamental parameters for each element (Flude et al., 2017), such as that from Elam et al. (2002). The final product for this study was elemental abundance in weight percent for Al, As, Ca, Fe, K, Mg, Mn, P, S, Si, and Ti, which were normalized to 100%, circumventing systematic geometric factor errors in calculating X-ray intensities (Elam et al., 2004).

Prior to quantification of study samples, the elemental compositions of test samples were quantified using various extraction methods offered in the Bruker M4 software. Quantification can be done on every pixel (1×1), or a grid of 3×3 , 5×5 , or 9×9 pixels. Quantifying in a grid acts to increase the X-ray counts for each quantified sample (grid of pixels), which decreases the spread of the dataset (Fig. 2). The trade-off is a loss in detail in the μXRF image as multiple pixels are combined. For this study, a 3×3 grid quantification (i.e., integrating spectra from 9 pixels) was selected to decrease the spread in data while maintaining sufficiently high spatial resolution to preserve textures and resolve fine-grained minerals in μXRF maps.

AMICS μXRF mineral identification

Bruker Advanced Mineral Identification and Characterization System (AMICS) is a software package for identification of mineralogy from Bruker M4 Tornado μXRF and SEM-electron dispersive X-ray spectroscopy (EDS) data. For mineral identification using μXRF datasets, full X-ray spectra are evaluated and compared to a library of known characteristic XRF spectra, using χ^2 fingerprinting for a best-match mineral classification. Mineral classification can be further refined using various clustering techniques and/or manual manipulation and evaluation of XRF spectral attributes (Bruker, pers. commun.). The final product is a dominant mineral-class map with one mineral-class label (single or specific mineral mixture) per pixel.

Micro-XRF-derived mineralogy from linear programming

The samples analyzed in this study are fine-grained sedimentary rocks where the average grain size is $<5 \mu\text{m}$. Therefore, many of the 100- μm μXRF sample points contain mineral mixtures. In order to predict mineral abundance, it is therefore necessary to estimate the mineral proportions within each pixel. Here we employ quantified μXRF results derived from the rock sample surface to predict and quantify mineral abundances using linear programming (LP), or linear optimization. Braun (1986) demonstrated that LP could be used to calculate mineral proportions of montmorillonite, quartz, and plagioclase from chemical data and X-ray diffraction (XRD) results. Linear programming is a mathematical method in which a series of variables are minimized or

maximized in order to reach an optimal solution given specific input constraints. In this case, LP is used to optimize the mineral proportions by calculating the proportion that makes use of the most geochemistry (maximization) within the constraints of the mineral formulae. This method has been shown to accurately calculate mineralogy in such applications as predicting acid rock drainage from multielement geochemistry (Berry et al., 2015), quantifying mineral contents of Martian soils (Cavanagh and Bish, 2016), and quantifying mineralogy of bentonites using multielement data (Braun, 1986).

Linear programming was used to calculate mineral abundances using quantitative geochemical results of μXRF analyses, using the lpSolve interface to Lp_solve v. 5.5 (Berkelaar, 2019) in the R statistical programming language (R Core Team, 2017). In this method, LP was used to maximize the mineral content (objective function) using the available geochemistry in the expression:

$$\max \{c^T x \mid Ax \leq b \wedge x \geq 0\},$$

where $c^T x$ is the objective function and the inequalities $Ax \leq b$ and $x \geq 0$ are the constraints for the optimization of the objective function. For this study, constraints for optimization include mineral stoichiometry (formulae derived from electron probe microanalyzer (EPMA) analyses), minerals present (as determined by XRD, mineral liberation analyzer (MLA), and EPMA), with constraints of a minimum value of zero (i.e., no minerals present), and maximum value of 100 (i.e., a sample is made up of only one mineral). This method produces multiple mineral labels with an estimated mineral proportion within each μXRF pixel.

External validation

Each of the 29 core samples ($\sim 8 \times 25 \text{ cm}$) that had been μXRF scanned were subsequently split so that one half could be crushed for validation work using homogenized powders. Each powder was scanned using the Bruker Tornado under the same operating conditions as the μXRF images. These powders were then fused into glass disks for analysis using laboratory wavelength dispersive spectroscopy XRF (WDS-XRF) on a Bruker S8 TIGER at the University of Waikato. Results of the WDS-XRF analyses were used to validate and calibrate μXRF quantitative results. Splits of the same powders were then used for quantitative powder X-ray diffraction (QXRD) analysis to quantify mineral abundances.

The second half of drill core samples were used for EPMA and MLA analyses. Microprobe EDS and WDS results and backscatter images were collected using the JEOL JXA-8530F Plus field emission electron microprobe (EPMA) at the University of Tasmania Electron Microscopy and X-ray Microanalysis Facility. An FEI MLA 650 ESEM at the same facility was used for finer scale mineral identification and mapping of three subsamples of μXRF -scanned rocks.

Reduced major axis (RMA) regression was used for independent variable comparisons (μXRF to WDS-XRF, whole-rock geochemistry to μXRF , and LP results to QXRD) due to the associated error of each variable and the assumption of symmetry between them (see Smith, 2009, for full description of RMA). WDS-XRF and whole-rock geochemical data were used to test the accuracy of the Bruker M4 μXRF FP data quantification method. The FEI MLA 650 ESEM was used to

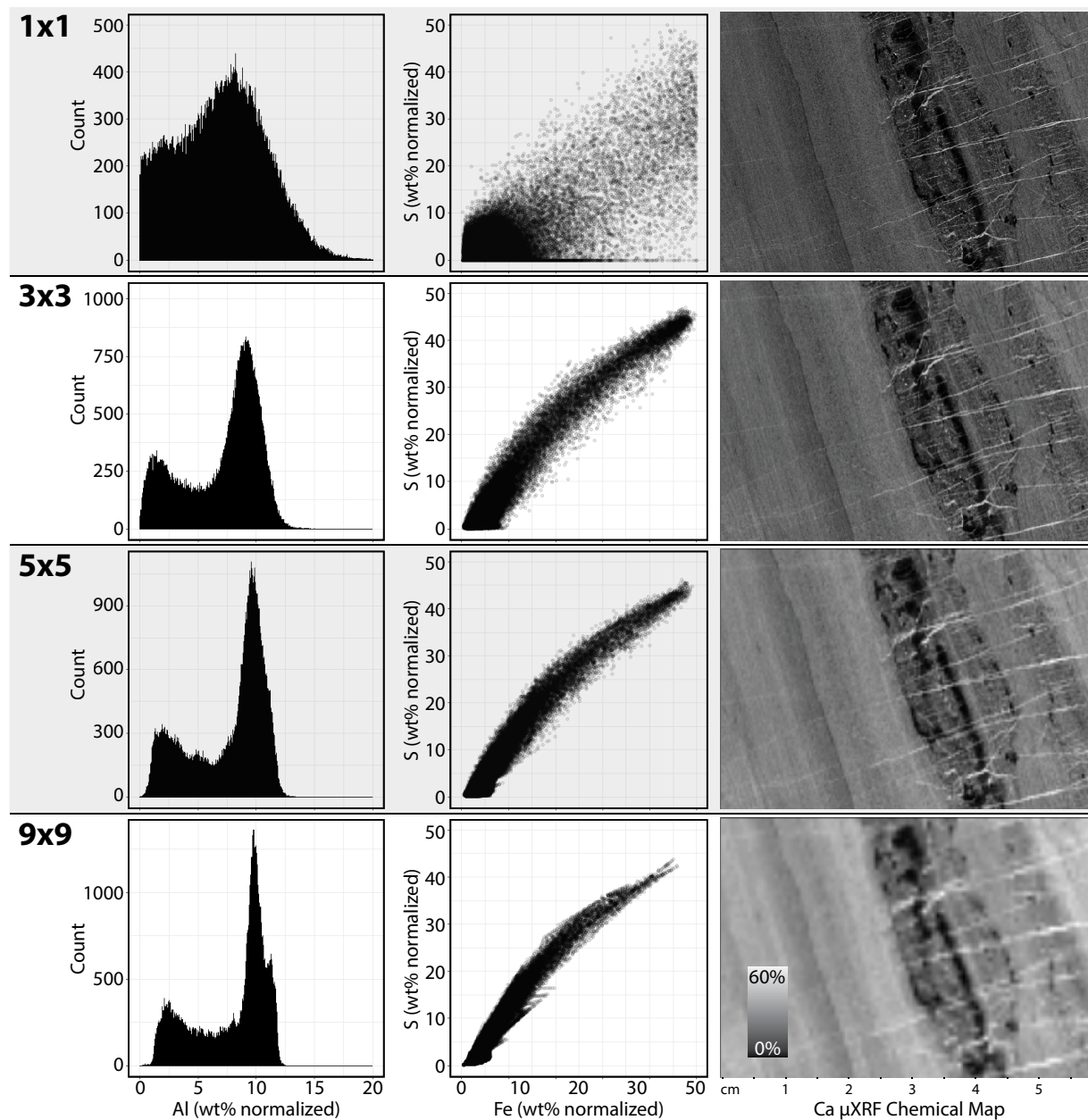


Fig. 2. Results of test quantification of micro-X-ray fluorescence (μ XRF) using various extraction grids of a hydrothermally altered rock sample. Quantification was done on individual pixels (1×1), and grids of 3×3 , 5×5 , and 9×9 pixels using the Bruker M4 software. The first column shows the distribution of Al with a sharpening of peaks with increase grid size. The second column is an S/Fe scatter plot of extracted elemental data from the sample shown in the images. Column three shows the μ XRF raster images of Ca with a decrease in textural information with increase in grid extraction size. The results show that extracting in a grid decreases the spread of the data and thus increases accuracy of the quantification. An increase in grid size also results in a loss of textural information in the μ XRF chemical maps, and loss in data related to fine-scale features such as the carbonate veins shown in the figures.

validate the qualitative mineral identifications from the μ XRF samples. XRD was used to identify minerals present for the LP algorithm and QXRD was used to assess the accuracy of the LP-derived mineral proportions.

Quantitative X-ray diffraction

Quantitative X-ray diffraction work was completed at the University of Alberta in the Environmental Economic Geology Laboratory. XRD data were collected in the Earth and

Atmospheric Sciences XRD Laboratory. A 2- to 3-g split from each of 18 powders scanned by μ XRF and WDS-XRF was ground under anhydrous ethanol with an McCrone micronizing mill for seven minutes, using agate grinding elements. Micronized samples were subsequently dried overnight then disaggregated and homogenized using an agate mortar and pestle.

A Ca exchange was performed on two samples that appeared to contain smectites (one contained smectite, the

other interstratified illite-smectite). This was done using the method described by Mervine et al. (2018) in order to stabilize the basal spacing of smectites to 15 Å, following the advice of Bish et al. (2003). It also assisted with distinguishing between smectite and illite-smectite. These two samples were suspended in 100 mL of 1 M CaCl₂ × 2H₂O (Fisher Chemical, Certified ACS grade), sealed in Schott bottles, and agitated vigorously overnight using an orbital shaker. Following agitation, samples were gravity filtered through filter paper (Whatman no. 1). Samples were rinsed 3× with deionized water. They were then dried overnight at room temperature and disaggregated with an agate mortar and pestle.

Powder XRD patterns were collected from front-loaded samples using a Rigaku Ultima IV θ - θ powder X-ray diffractometer equipped with a D/Tex Ultra detector and a cobalt source that was operated at 38 kV and 38 mA. XRD patterns were collected from 5°–80° 2 θ using a step size of 0.02° 2 θ at a rate of 2° 2 θ /min. For the two samples containing smectite or illite-smectite, relative humidity was recorded before and after each pattern was collected and a humidifier was run during sample analysis to maintain relative humidity in the range of 20 to 80% (after Bish et al., 2003).

Qualitative phase identification was conducted using the DIFFRAC.EVA XRD phase analysis software (Bruker) with reference to the International Center for Diffraction Data Powder Diffraction File 4+ database (ICDD PDF4+). Rietveld refinement (Rietveld, 1969; Hill and Howard, 1987; Bish and Howard, 1988) with XRD data was done to estimate mineral abundances using TOPAS 5 (Bruker). The fundamental parameters peak fitting protocol of Cheary and Coelho (1992) was used for all phases. Three samples produced patterns with significant anisotropic peak broadening in either calcite or dolomite; in the one instance that involved calcite, the model of Stephens (1999) was used to account for this effect, in the other two, a far better fit was obtained using two compositionally distinct structures for dolomite (i.e., one “high Ca,” one “low Ca”). The partial or no known crystal structure (PONKCS; Scarlett and Madsen, 2006) method of structureless fitting was used to model the peak profiles of kaolinite (where present at approx ≥ 10 wt %) and montmorillonite (wherever present) to account for turbostratic stacking disorder. The use of Rietveld-compatible structureless fitting methods, such as PONKCS, can result in overestimates of the structurally disordered phases for which they are used, owing to overestimation of peak intensities at the expense of other phases with overlapping peaks (Wilson et al., 2006; Turvey et al., 2018). This effect is particularly notable at low abundances; as such, where kaolinite was present at <10 wt %, the standard Rietveld approach for phase quantification (Hill and Howard, 1987; Bish and Howard, 1988) was used instead.

Elemental abundances were forward calculated from QXRD modal mineralogy using mineral formulae determined with EPMA results. The QXRD-derived chemistry was subsequently compared to whole rock XRF data for validation of QXRD results. As this study is focused on identifying typical Carlin-type mineral assemblages, metasomatic minerals and low abundance (<1%) phases identified using XRD data, such as actinolite, phlogopite, anorthite, siderite, hematite, anatase, and smectite, were not included in the μ XRF maps presented; however, they were used to calculate elemental

abundances for validation of QXRD results by comparison with XRF results.

Results

Micro-XRF geochemistry results and interpretation

Micro-XRF geochemical images show the relative variations of chemistry in a rock sample which, in turn, reflect the variations in mineralogy. For example, Figure 3A shows the μ XRF-derived relative concentrations of Ca, Mg, and Mn of sample M180080, which are interpreted to reflect the presence and compositions of the carbonate minerals, dolomite and calcite, of this hydrothermally silicified limey mudstone. The sample has a complex network of crosscutting carbonate veinlets that appear to be syn- and postdecalcification. A comparison of the three-element μ XRF image (Fig. 3A) to the true-color image (Fig. 3B) of the same sample illustrates that the hand sample has no visible indication of the variation of carbonate mineral chemistry within the veins. EPMA analyses and EPMA backscatter electron (BSE) images (Fig. 3C, D) confirm the presence of dolomite, Mg-Mn-calcite, and calcite in this sample, consistent with the μ XRF image.

Figure 4 shows sample M180095, a limey mudstone sample with pervasive hydrothermal argillization and minor sulfidation and silicification. This sample reveals the relationship between μ XRF-derived relative concentrations of K (cyan) and Al (red) (Fig. 4A), which is interpreted to reflect K-bearing (illite, and K-feldspar) and non-K-bearing aluminosilicates (e.g., kaolinite). Differences in the color, and its intensity, within grains and veins in Figure 4A and B reflect the variable K/Al ratio of these minerals. Thus, bright cyan represents the highest K/Al ratio (K-feldspar), light cyan to white shows a lower K/Al ratio (illite) and red shows the absence of K (kaolinite). In Figure 4A, K-feldspar is found primarily within breccia clasts, illite can be seen along fractures and in the breccia matrix, and kaolinite is primarily confined within the lower right corner of the image. Figure 4B is a true-color image of the same sample for comparison. Potassium feldspar, illite, and kaolinite were also identified in this sample using an MLA mineral map (Fig. 4C) and EPMA (EDS and EPMA-BSE imaging; Fig. 4D).

Micro-XRF fundamental parameters standardless quantification

In order to assess the accuracy of the fundamental parameters method, quantified μ XRF results for major rock-forming elements (Al, Ca, Fe, K, Mg, and Si) were compared to the results of calibrated WDS-XRF analyses on glass disks created from the same powdered samples (Fig. 5). The R² values of 0.98 to 0.97 and intercepts near 0 suggest that the standardless FP method provides precise quantitative chemical results that can be used to estimate the abundance of mineral phases. The results of the RMA line for each element were used to correct the μ XRF FP results for subsequent LP mineral calculations.

AMICS μ XRF mineral identification

Figure 6 shows AMICS software results for mineral identification from the same sample seen in Figure 3 (sample M180080). This is a dominant mineral map where each pixel is labeled with a single mineral class (representing one or more minerals). The mineral map in Figure 6 highlights key

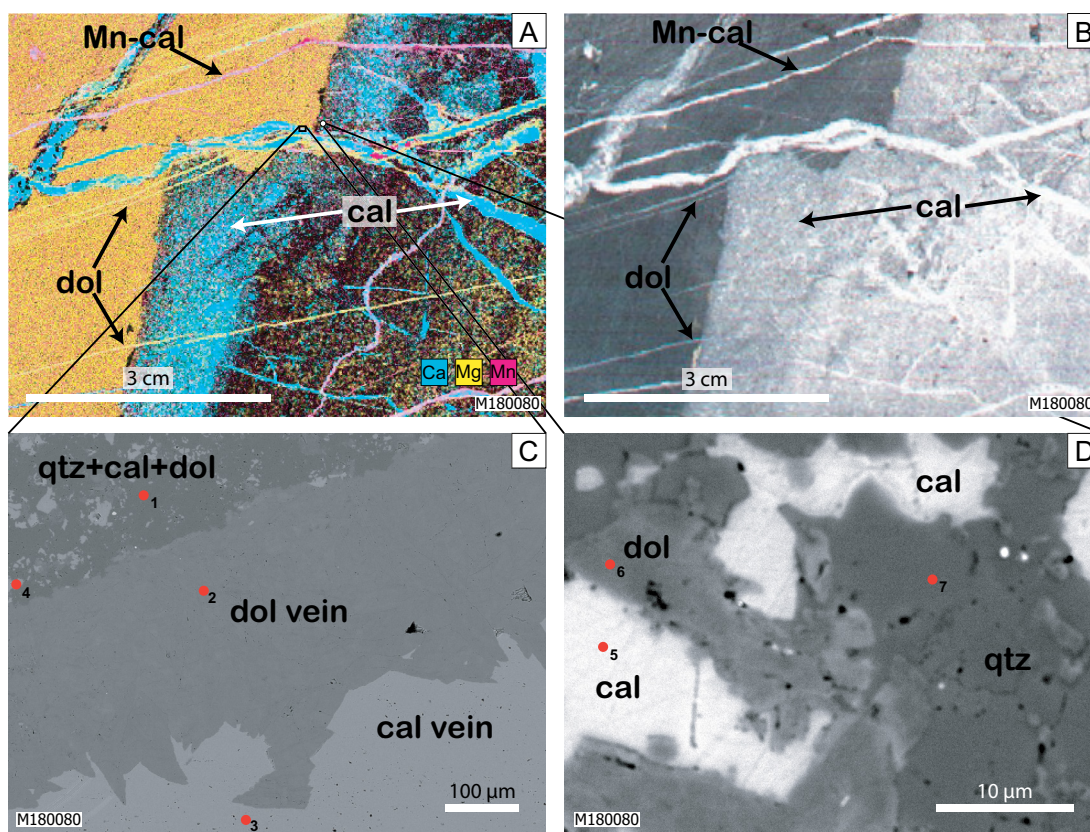


Fig. 3. A. Micro-X-ray fluorescence (μ XRF) image of sample M180080 as a three-element overlay that includes Ca, Mg, and Mn. This sample is a hydrothermally silicified limey mudstone. The colors depict each element and the intensity of each color is a representation of the relative concentration (unitless). For example, strong intense cyan indicates relatively high concentrations of Ca, which in turn are interpreted to reflect the presence of calcite. Pink indicates a mix of Ca and Mn which is interpreted to be Mg-Mn calcite veinlets. These elements are interpreted to reflect variations in the carbonate mineralogy, which includes calcite, dolomite, and Mn-Mg-calcite. The box and dot show the estimated locations of the backscatter electron (BSE) samples relative to the μ XRF. B. True-color image of the same sample as in (A), a test sample used for validation of predicted μ XRF mineralogy results. C. and D. Electron probe microanalyzer (EPMA)-BSE images of sample from (A) and (B). Red circles with numbers represent EPMA analytical locations with results given in Table 2. Abbreviations: cal = calcite, dol = dolomite, qtz = quartz.

mineral assemblages such as that associated with the host rock (calcite-illite-dolomite-quartz), silicification and decalcification (quartz and calcite-quartz), chlorite alteration of the host rock (illite-chlorite-calcite-quartz), and hydrothermal veins (calcite, pyrite, Fe dolomite, Mn calcite).

A breakdown of mineral assemblages, along with the XRF spectral signature that represents each assemblage in AMICS for the hydrothermally altered sample M180080 (Fig. 7), also shown in Figures 3 and 6, illustrates that the mineral assemblage XRF photon energies of principal $K\alpha$ X-ray lines (keV) are mostly consistent with the elemental signatures of the minerals identified (Willis et al., 2011). There are, however, some X-ray peaks that are unaccounted for in mineral classes such as pyrite, where the detection of Si and Ca suggests that there is contamination of the representative pyrite spectra with the chemical elements that make up surrounding matrix minerals.

Linear programming (LP) μ XRF mineral identification and quantification

The LP approach to mineral quantification allows the abundance of each mineral in each μ XRF pixel to be estimated,

as opposed to the AMICS approach where pixels are given either single mineral or mineral mixture labels. The following results of the quantitative LP mineralogy estimates are from hydrothermally altered μ XRF core samples. The LP mineral results were qualitatively validated using MLA and EPMA-BSE images from the same samples.

Figure 8 is a breakdown of the results of LP-derived mineralogy for sample M180080, which is also shown in Figures 3, 6, and 7. The results show that the LP method can be used to quantify calcite, dolomite, illite, pyrite, and quartz and that the textures in each mineral map are consistent with that of hydrothermally altered rock from Carlin-type gold deposits (Cline et al., 2005; Cline, 2018), revealing alteration textures such as silica replacement of calcite (silicification and decalcification, Fig. 8A, E) and the presence of carbonate veins (Fig. 8A, B). When coupled with the quantitative chemical data, the calcite veins were subdivided into Mn calcite, Mg calcite, and Fe calcite (Fig. 8F).

An LP-derived illite, calcite, and quartz composite image of a silicified carbonaceous limey mudstone breccia sample shows that calcite occurs within the limestone host rock and veins, and lower calcite abundances are consistent with

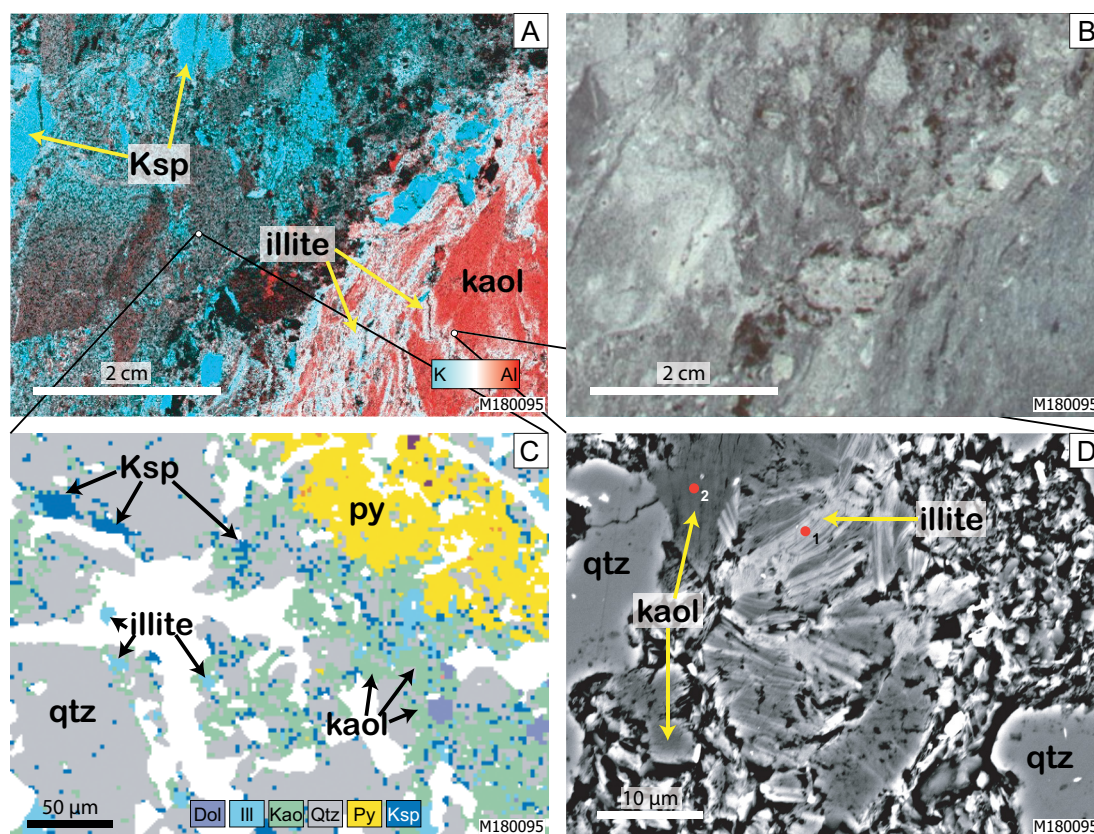


Fig. 4. Micro-X-ray fluorescence (μ XRF) map showing relative concentrations of Al and K (unitless) in sample M180095, a limy mudstone with pervasive hydrothermal argillization and minor sulfidation and silicification. The Al and K in this sample are interpreted to reflect the aluminosilicate mineralogy, which includes kaolinite, illite, and K-feldspar. The element overlay map provides an estimated location and alteration patterns of illite (indicated by white color) and K-feldspar (cyan). The mixture (additive) of cyan and red (complementary colors) in roughly equal proportions creates white, which reflects illite (K/Al ratio of ~ 0.67), while K-feldspar is shown as cyan (K/Al ratio of ~ 1.45) and kaolinite is shown in red (no K). It is important to note that these are relative abundances and there is a color stretch applied to the images which means that, while there is Al in K-feldspar, relative to the rest of the sample, K is dominant in this region and is expressed as almost pure cyan. White dots indicate the location from which the mineral liberation analyzer (MLA) and backscatter electron (BSE) figures were sourced relative to the μ XRF. B. True-color image of the same sample as in (A). C. MLA mineral map of sample from (A). D. Electron probe microanalyzer (EPMA)-BSE image of sample from (A). Red circles with numbers represent EPMA locations with results given in Table 2. Abbreviations: kaol = kaolinite, Ksp = K-feldspar, py = pyrite, qtz = quartz.

decalcification within and adjacent to the breccia (Fig. 9A). Illite is disseminated in the sedimentary rock of the sample and is enriched along the contact between a breccia and siltstone. Quartz abundance in this mineral map is interpreted to reflect hydrothermal silicification, as well as diagenetic quartz grains in the sedimentary rock. Similar mineralogical results are seen in the MLA image of the same sample (Fig. 9B); however, the MLA map contains a single label per pixel rather than multiple labels with mineral abundance.

A transect of quartz concentration from sample M180080 shows the location of silicification, as well as the gradational decrease in quartz moving away from the breccia into the adjacent rock (Fig. 9C). Overall, these images reveal in detail similar mineralogy and rock textures (e.g., decalcification and silicification) to those described for Carlin-type hydrothermal gold deposits elsewhere in Nevada (Emsbo et al., 2003; Cline et al., 2005; Vaughan et al., 2016).

The distribution of potassium feldspar and kaolinite were also calculated using LP (Fig. 10A). Figure 10A shows an LP-derived mineral map of illite, kaolinite, and K-feldspar as

predicted from μ XRF data. The LP results are consistent with the mineral textures identified in the MLA (Fig. 10B), and EPMA-BSE (Fig. 10C), which consists of fine-grained intermix of these three mineral phases. Electron probe microanalyses (Fig. 10D-F), confirm the presence of these minerals. This sample contains a silicification front with kaolinite disseminated throughout the sample, with illite and K-feldspar mostly confined to the unsilicified portion.

Validation of quantitative mineralogy derived from linear programming

Carbon concentrations were predicted from μ XRF LP-derived mineralogy results (note that C is not measured by the μ XRF instrument used in this study) and were compared to total carbon results from whole-rock geochemical analyses of the split core samples (Fig. 11). While this approach does not consider any potential organic carbon contribution to total C in the whole-rock samples, the concentration of carbonate minerals is likely much greater than organic C and thus organic carbon likely has a relatively minor impact on the results of

Table 2. EPMA Results of Points Shown in EPMA-BSE Figures

Sample	Site	Type	Si (wt %)	Ti (wt %)	Al (wt %)	Fe (wt %)	Mn (wt %)	Mg (wt %)	Ca (wt %)	Sr (wt %)	Ba (wt %)	Na (wt %)	K (wt %)	F (wt %)	C (wt %)	O (wt %)	Total (wt %)
M180080	1	EDS	46.32	0.00	0.00	0.00	0.00	0.00	0.28	0.00	0.00	0.00	0.00	0.00	NA	53.40	100.00
M180080	2	EDS	0.47	0.00	0.00	1.18	0.00	13.98	30.22	0.00	0.00	0.00	0.00	0.00	NA	54.15	100.00
M180080	3	EDS	0.00	0.00	0.00	0.00	0.00	0.57	54.52	0.00	0.00	0.00	0.00	0.00	NA	44.91	100.00
M180080	4	EDS	0.00	0.00	0.00	0.00	0.00	0.39	48.95	0.00	0.00	0.00	0.00	0.00	NA	50.67	100.00
M180080	5	WDS	0.68	0.03	0.39	1.20	0.06	13.09	20.42	0.04	0.02	-0.01	0.25	NA	12.97	52.87	102.00
M180080	6	WDS	0.12	0.00	0.05	0.06	0.05	0.33	40.20	0.03	0.05	0.01	0.06	NA	11.94	48.32	101.22
M180080	7	EDS	46.04	0.00	0.00	0.00	0.00	0.00	0.36	0.00	0.00	0.00	0.00	0.00	NA	53.60	100.00
M180095	1	EDS	24.39	0.00	19.18	0.00	0.00	0.35	0.00	0.00	0.00	0.00	6.78	0.00	NA	49.30	100.00
M180095	2	EDS	22.99	0.00	20.77	0.00	0.00	0.00	0.00	0.00	0.00	0.00	0.00	0.00	NA	56.25	100.00
M180130	1	WDS	23.78	0.19	16.26	1.69	0.01	1.18	0.18	-0.01	0.10	0.16	8.70	0.06	NA	44.83	97.12
M180130	2	WDS	21.77	0.03	19.61	0.29	0.01	0.30	0.18	0.00	0.06	0.01	1.84	0.01	NA	43.00	87.11
M180130	3	WDS	30.28	0.01	9.84	0.04	-0.01	0.02	0.19	-0.01	0.03	0.10	13.34	-0.02	NA	46.13	99.94

BSE = backscatter electron, EDS = electron dispersive X-ray spectroscopy, EPMA = electron probe microanalyzer, WDS = wavelength dispersive spectrometry; EDS totals are normalized to 100%

this comparison. The high RMA R² value of 0.87, the slope of the RMA line near one (m = 1.11), and the intercept near zero (b = -1.1) shows that the LP prediction for carbonate (calcite and dolomite) mineral abundances are accurate for most samples, which suggests that the organic C assumption is reasonable. An outlier in Figure 11 has been overestimated in the mineral model compared to whole-rock LECO analysis. This may be due to a higher than normal contribution to Ca from minerals not included in the LP calculations, such as wollastonite, and not likely due to the presence of organic C due to the lack of organic C in this metacarbonate sample. The Ca in wollastonite of the outlier sample would cause an overestimate of C because Ca is assumed to be primarily within carbonate minerals.

Quantitative X-ray diffraction (QXRD) was completed on selected μ XRF samples for the purpose of validating μ XRF-derived LP mineralogy results. Weighted pattern residual values, R_{wp}, for Rietveld refinements ranged from 1.9 to 6.0%, indicating good model fits to the observed data. It is important to note that the absolute and relative error on mineral abundances, as estimated from Rietveld refinement results, is typically greater at lower mineral abundances (e.g., Wilson et al., 2006, 2009). Root mean square error (RMSE) for chemical compositions calculated using QXRD results compared to quantified whole-rock μ XRF results range from 0.42 (S) to 6.94% (SiO₂) (Table 3). The moderate to high correlation coefficient (R²) and regression line near y = x show that QXRD and μ XRF analyses agree. Finally, mineral abundances predicted from μ XRF data using the LP method are consistent with QXRD results, shown by high R² (0.82–0.97) and regression lines (QXRD vs. LP) near y = x (Fig. 12). Using QXRD as a baseline for comparison, RMSE for LP-derived mineralogy ranges from 0.91 (pyrite) to 7.15% (dolomite).

Discussion: Micro-XRF Geochemistry Results and Interpretation

The strength of the μ XRF chemical mapping technique is in its ability to scan large core samples relatively quickly to reveal geochemical textures in rock samples that cannot be seen with the unaided eye (Ryan et al., 2018). An example is seen in Figure 3A and B that shows a μ XRF chemical map for Ca, Mg, and Mn of a hydrothermally altered rock sample next to a true-color image of the same sample. The μ XRF image shows many variations in the elemental composition of carbonate

Table 3. Calculated Geochemistry for Major Elements from QXRD Results Compared to Quantified WDS-XRF from the Same Samples as in Figure 5 for the Purpose of Validating QXRD Results (S results from quantified μ XRF and CO₂ calculated for XRF from CaO and MgO)

	RMSE	R ²	Slope	Intercept
Al ₂ O ₃	2.75	0.78	0.79	1.04
CaO	4.71	0.97	0.85	0.62
FeO	1.53	0.97	1.07	1.06
K ₂ O	0.75	0.86	1.17	0.38
MgO	1.71	0.88	0.86	1.03
S	0.42	0.9	0.85	0.09
SiO ₂	6.94	0.95	1.06	2.69
CO ₂	3.91	0.92	1.02	-0.32

QXRD = quantitative X-ray diffraction, WDS = wavelength dispersive spectrometry, μ XRF = micro-X-ray fluorescence

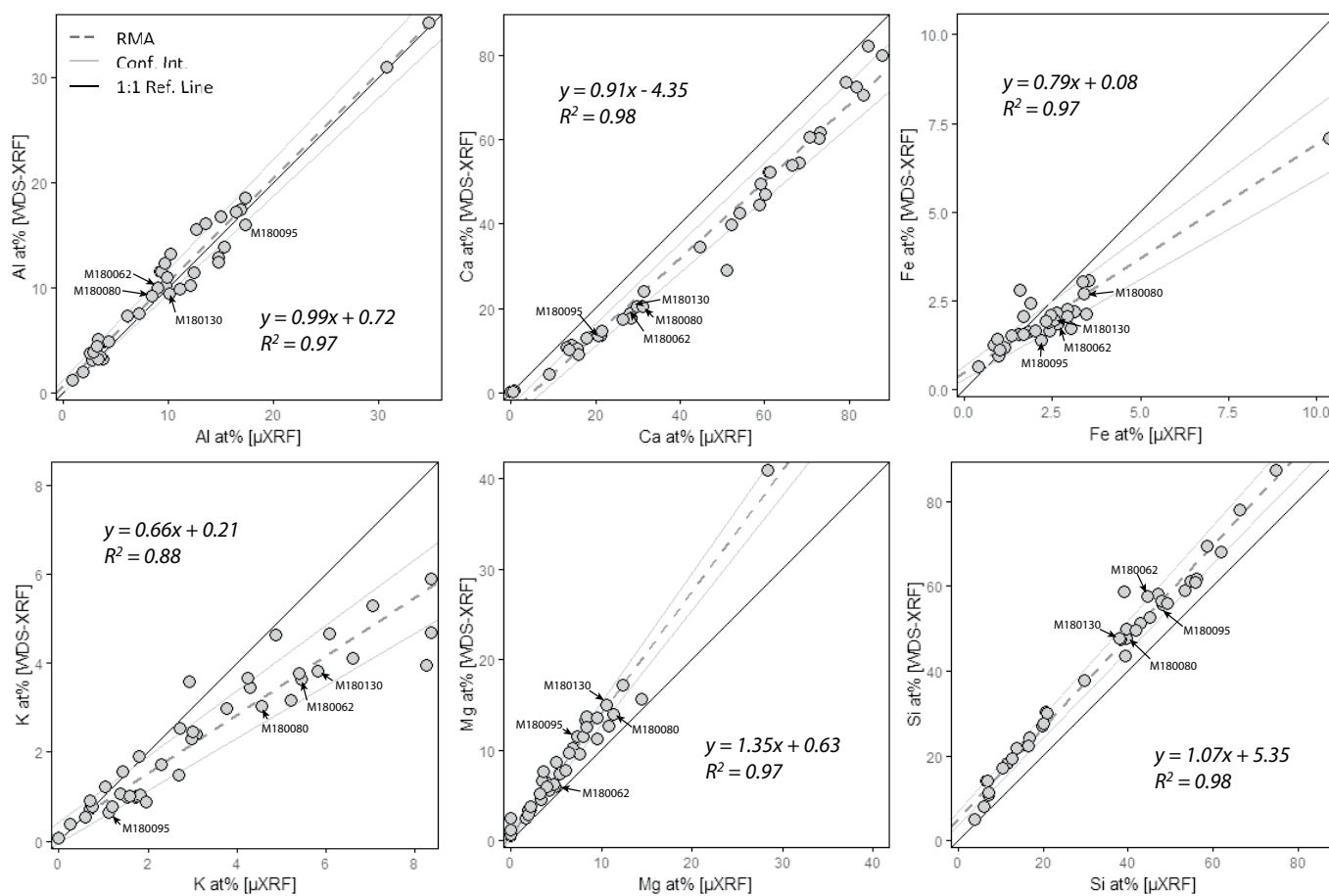


Fig. 5. Abundances of individual elements Al, Ca, Fe, K, Mg, and Si obtained from μ XRF analyses compared to those obtained via WDS-XRF in atomic percent. Dashed line represents the RMA regression line between measured values. Thin gray lines represent the 95% confidence intervals. The thin black line shows the 1/1 line. Linear equation and R^2 value inset for RMA line. RMA = Reduced major axis, WDS = wavelength dispersive spectrometry, μ XRF = micro-X-ray fluorescence.

veins and host-rock carbonate that are not obvious in the true-color image. This may be of use in exploration when the carbonate vein composition can provide vectors toward mineralization such as that of the Mn calcite vein shown to be associated with mineralization in a Carlin-type deposit in

the Yukon (Steiner and Hickey, 2019). Micro-XRF composite chemical maps can also reflect specific mineralogy such as that of the K-Al maps that are interpreted to show illite, K-feldspar, and kaolinite (Fig. 4). Because of the fine scale of the μ XRF beam, and the scale over which that beam can

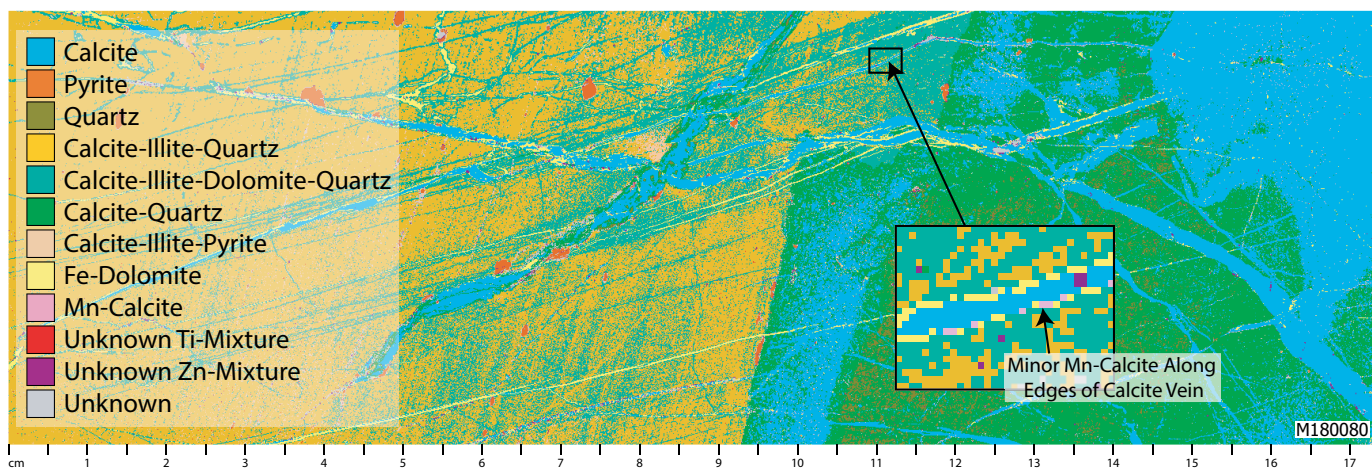


Fig. 6. Mineral map derived from μ XRF = micro-X-ray fluorescence, using Bruker AMICS mineral identification software for sample M180080, a limey mudstone with hydrothermal silicification.

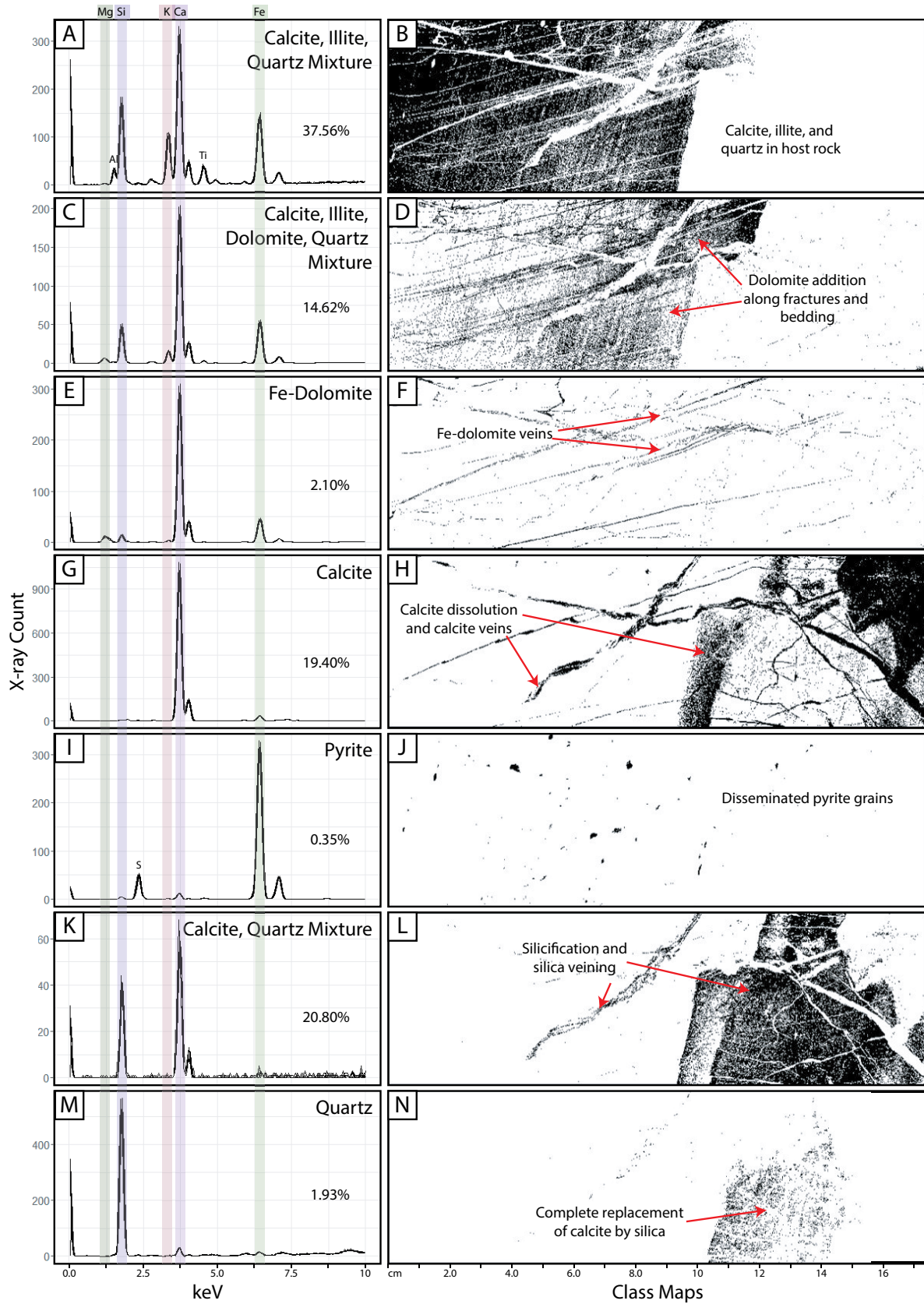


Fig. 7. Breakdown of mineral classes (shown as black dots where present in samples) accompanied by X-ray fluorescence spectral signature as identified by the Bruker AMICS mineral identification software for sample M180080. Compare results to Figures 3A-D and 6. Percentage values shown for each mineral class are the area percent of each class identified in this sample.

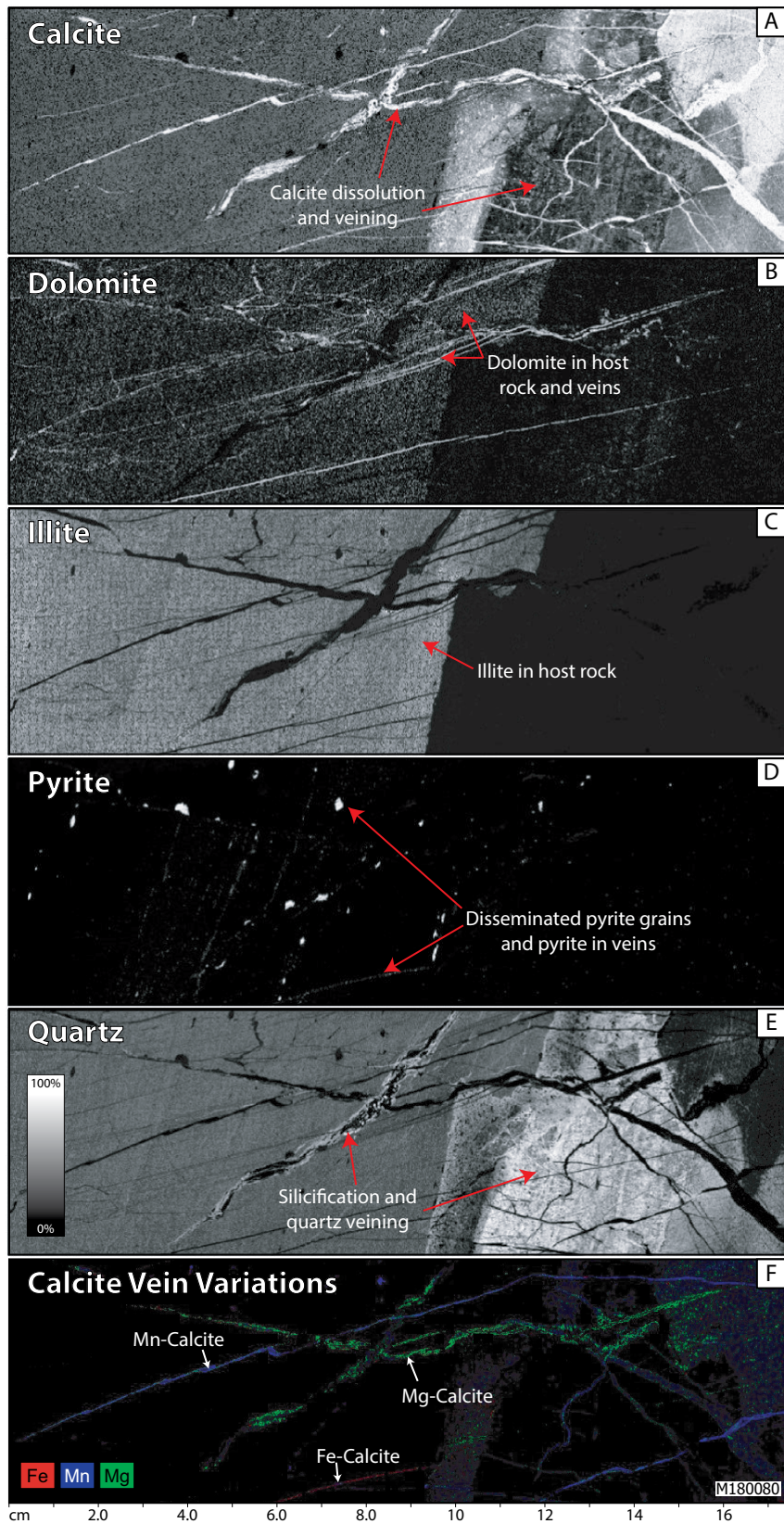


Fig. 8. A.-E. Breakdown of linear programming-derived quantitative mineralogy results of μ XRF sample M180080 seen in Figures 3A-D, 6, and 7. Each mineral map shows absolute mineral proportions. Abundance scale applies to (A-E). F. Geochemical maps of pixels identified to have more than 50% calcite that show three variations of calcite veins, Mn calcite (blue), Mg calcite (green), and Fe calcite (red).

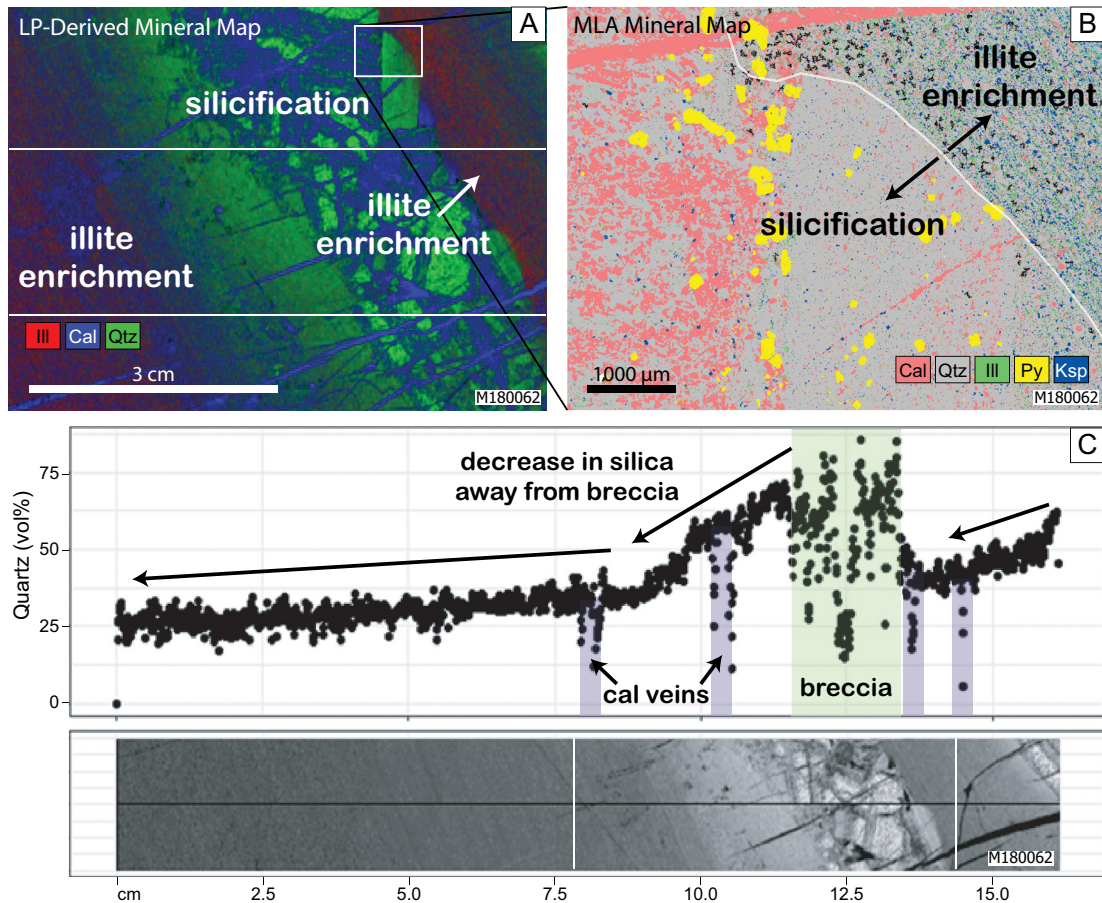


Fig. 9. A. Micro-X-ray fluorescence (μ XRF)-derived relative quantity mineralogy map (unitless) for quartz (green), calcite (blue), and illite (red), showing carbonate replacement by silica (silicification and decalcification) preferentially along bedding and brecciation of sample M180062. B. Mineral liberation analyzer (MLA) mineral map of sample shown in (A) with illite enrichment, silica from silicification, and calcite. White line drawn in to highlight contact between silicification and illite enrichment. C. Transect of μ XRF-derived mineralogical map of quartz from sample in (A) and (B) that shows a gradual increase in quartz abundance approaching the breccia. White lines in (A) and (C) show the boundaries of overlap between the two figures. The white box in (A) shows the location of the MLA scan shown in (B).

be rastered (~ 50 cm), fine-scale mineralogical variations can be evaluated on a relatively large scale across a rock sample compared to what can be achieved using thin-section and SEM techniques. Thus, significantly more chemical and textural information can be gleaned for the purpose of identifying associations of ore and alteration minerals. In addition, μ XRF scanners allow more representative selection of rock samples or drill core and make sampling bias less likely due to the larger sampling volumes compared to other analytical methods such as SEM or EPMA.

Conclusion: Comparison of AMICS and Linear Programming for Mineral Identification

In fine-grained samples, the AMICS software identifies mineral groups (mixtures), such as those related to lithology (calcite-illite-quartz), hydrothermal alteration of the host rock (calcite-illite-dolomite-quartz, and calcite-quartz), and those pixels that fall along grain boundaries (calcite-illite-pyrite). If the grain sizes are larger than the pixel size, or there are large enough numbers of fine-grained minerals in a spatial cluster, the mineral class will be of a single mineral (calcite, pyrite,

quartz, Fe dolomite, and Mn calcite). However, even those mineral classes that were identified as a single mineral (i.e., pyrite) have photon energy peaks from additional elements (e.g., Ca and Si). As there is no way to classify the vast number of possible mixture variations when three or four minerals may be mixed together, mineral mixtures for fine-grained samples cannot be accurately quantified using the AMICS method. In this case, the LP method offers significant advantages in that it can be used to quantify mineral mixtures. The LP method produces multiple mineral labels and abundances for each pixel, whereas AMICS provides a single label per pixel.

A potential drawback to calculating mineralogy using LP can be seen in the lower correlation coefficients of illite and K-feldspar predictions compared to QXRD results from the same samples. Because the chemical compositions of illite and K-feldspar are similar, when both minerals are present in a sample, especially in the presence of quartz and kaolinite, it is difficult to distinguish variations in the abundance of these phases. Potentially these results can be improved if the LP method was coupled with other mineral identification methods, such as LWIR or SWIR spectroscopy and/or qSEM.

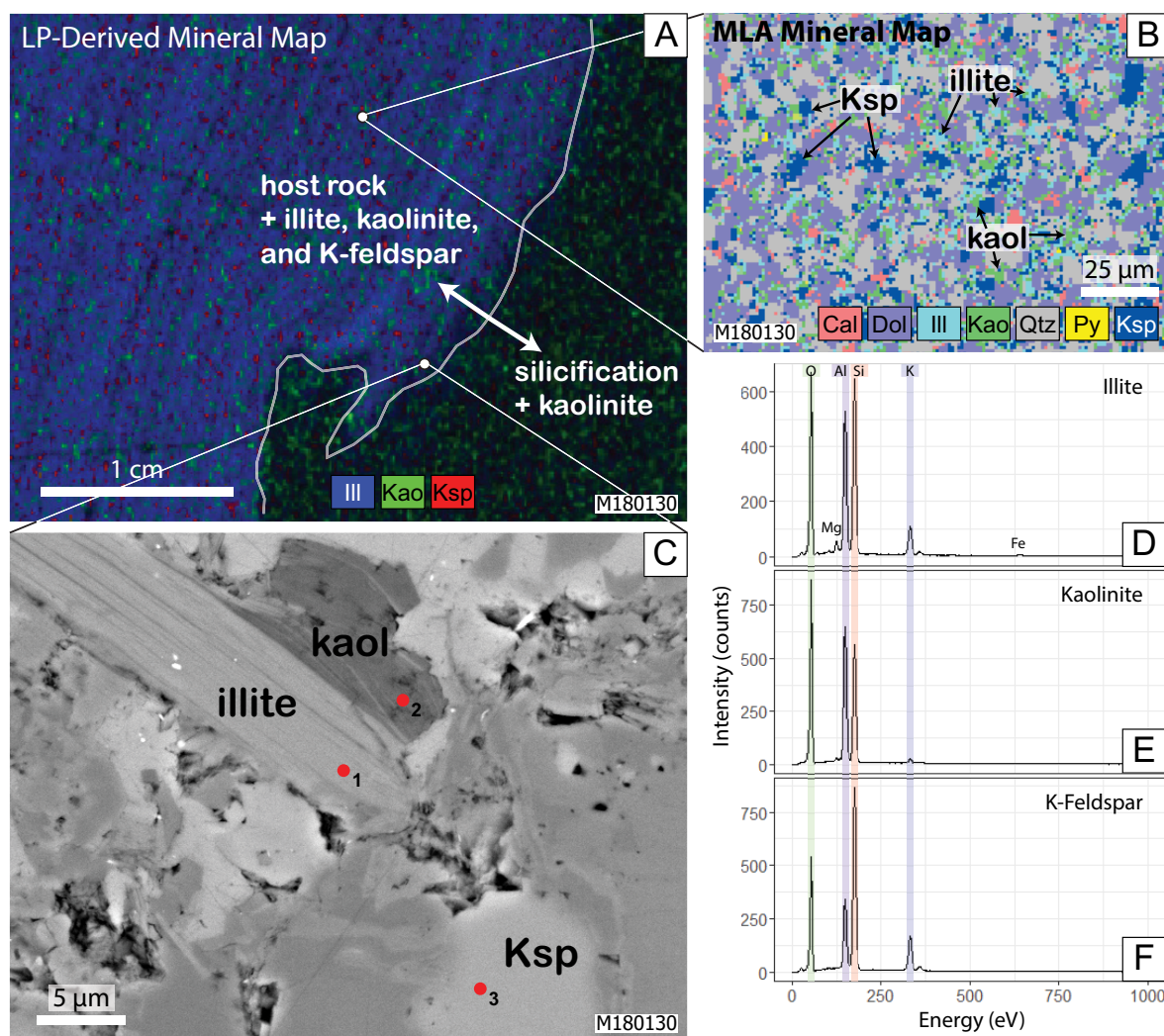
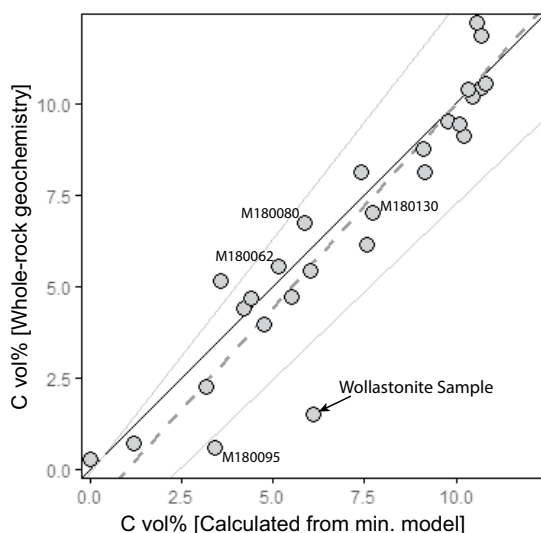


Fig. 10. A. Micro-X-ray fluorescence (μ XRF)-derived linear programming(LP) mineral map of sample M180130 with illite (blue), kaolinite (green), and K-feldspar (red). White line drawn to show contact between silicification and host rock. White dots show the estimated location of the Mineral liberation analyzer (MLA) and backscatter electron (BSE) images relative to the μ XRF. B. MLA mineral map of the same sample, which shows mineralogy consistent with that identified with the LP method. C. Electron probe microanalyzer (EPMA)-BSE image with EPMA points (red) that reflect similar mineralogy. D.-F. EPMA-EDS data for the three points from (C).



The approach outlined here demonstrates that μ XRF maps can be used to determine mineralogy, mineral abundances, and mineralogical textures not visible with the naked eye from fine-grained sedimentary rocks associated with Carlin-type Au deposits. This approach is transferable to any ore deposit, but particularly sedimentary-hosted ore deposits where ore and gangue minerals are commonly fine grained and difficult to distinguish in hand specimen. Ultimately, improving our ability to map and predict the distribution of minerals within ore deposits is beneficial for improving our understanding of deposit genesis, recognizing the distribution of ore minerals and associations of ore and gangue minerals, as well as

Fig. 11. Carbon from LECO analysis vs. carbon calculated from carbonate results of micro X-ray fluorescence-derived linear programming mineralogy. Dashed line represents the reduced major axis regression line between measured values. Thin gray lines represent the 95% confidence intervals. The thin black line shows the 1/1 line.

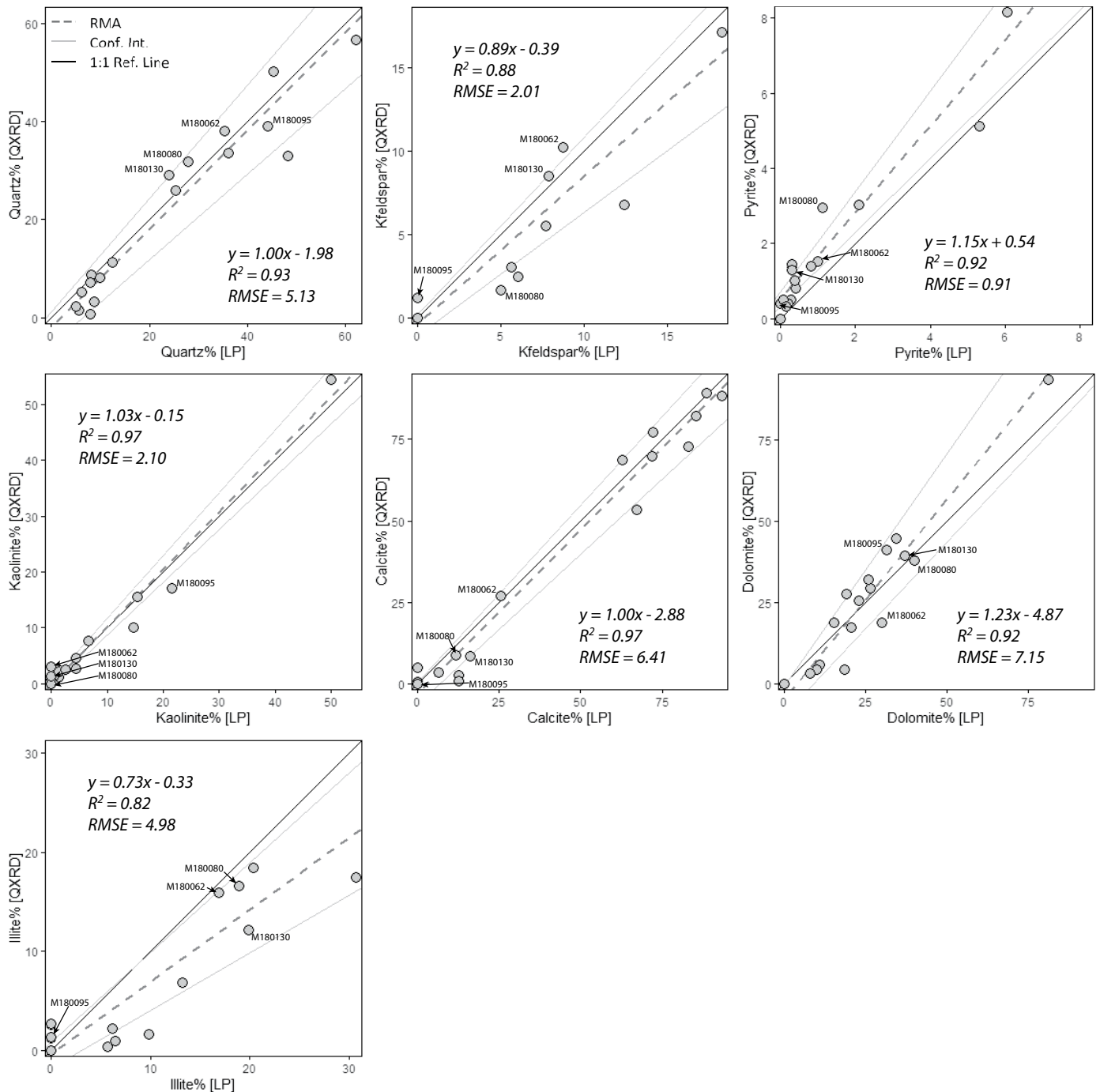


Fig. 12. Quantitative X-ray diffraction (QXRD) results compared to linear programming (LP) results for quartz, K-feldspar, pyrite, kaolinite, calcite, dolomite, and illite. R^2 , slope, and intercept values of reduced major axis (RMA) regression line shown in each plot. Points from micro-X-ray fluorescence (μ XRF) samples of this study that were analyzed using QXRD are highlighted for each plot for reference to the μ XRF, mineral liberation analyzer, and backscatter electron figures.

understanding and predicting how mineralogy may influence ore processing.

Acknowledgments

Thank you to Jared Janzen and Rebecca Funk from the University of Alberta for micronizing samples and for collecting XRD patterns, respectively. Thank you to the Bruker M4

team and to Gerda Gloy with the Bruker AMICS team for use of the M4 software and AMICS software packages, as well as being available for tech support and software-related questions. Thanks to Karsten Goemann and Sandrin Feig of the Central Science Laboratories at the University of Tasmania for assistance with MLA and EPMA analyses. We would like to acknowledge the insights of Ron Berry for thought-provoking and stimulating conversations regarding mineral

calculation from geochemistry. Finally, we would like to thank Barrick Gold Exploration Inc. and the University of Waikato Doctoral Scholarship program for sponsoring this research.

REFERENCES

- Ahmed, A.D., Hickey, K.A., and Barker, S.L.L., 2010, The Elder Creek deposit: The upper plate expression of an auriferous Carlin-type hydrothermal system?, in Steininger, R., and Pennell, B., eds., *Great Basin evolution and metallogeny: Geological Society of Nevada Symposium Volume*, Reno, Nevada, May 2010, p. 909–926.
- Barker, R.D., 2017, Geochemical and mineralogical investigation of breccias at the El Niño Au-Ag deposit, Elko County, Nevada: M.Sc. thesis, Fort Collins, Colorado, Colorado State University, 221 p.
- Berkelaar, M., 2019, lpSolve: Interface to 'Lp_solve' to solve linear/integer programs: v. 5.5 (<https://github.com/gaborcsardi/lpSolve>)
- Cavanagh, P. D., and Bish, D. L., 2016, Linear programming approach to quantitative mineralogy on Mars: 47th Lunar and Planetary Science Conference: Woodlands, Texas, USA, March 2016, p. 1-2.
- Tagle, R., and Reinhardt, F., 2016, Standardless and standard-supported fundamental parameter quantification of steel samples: Bruker Lab Report XRF 465, 4 p. (https://www.bruker.com/fileadmin/user_upload/8-PDF-Docs/X-rayDiffraction_ElementalAnalysis/mXRF/LabReports/LR_m4_tornado_xrf_465_steel_quantification_lores.pdf)
- Berkelaar, M., 2019, lpSolve: Interface to "Lp_solve" to solve linear/integer programs (v. 5.5): <https://github.com/gaborcsardi/lpSolve>.
- Berry, R., Hunt, J., Parbhakar-Fox, A., and Lottermoser, B., 2015, Prediction of acid rock drainage (ARD) from calculated mineralogy: International Conference for Acid Rock Drainage, 10th Santiago, Chile, April 2015, Proceedings, p. 1–10.
- Bish, D.L., and Howard, S.A., 1988, Quantitative phase-analysis using the Rietveld method: *Journal of Applied Crystallography*, v. 21, p. 86–91.
- Bish, D.L., Carey, J.W., Vaniman, D.T., and Chipera, S.J., 2003, Stability of hydrous minerals on the Martian surface: *Icarus*, v. 164, no.1, p. 96–103.
- Braun, G., 1986, Quantitative analysis of mineral mixtures using linear programming: *Clays and Clay Minerals*, v. 34, p. 330–337.
- Bruker, 2018a, M4 Tornado AMICS, (<https://www.bruker.com/products/x-ray-diffraction-and-elemental-analysis/micro-xrf-and-txrf/m4-tornado/m4-tornado-amics.html>).
- 2018b, ESPRIT 2: Software for micro- and nano-analysis, (<https://www.bruker.com/products/x-ray-diffraction-and-elemental-analysis/eds-wds-ebstd-sem-micro-xrf-and-sem-micro-ct/esprit-2.html>).
- 2018c, M4 Tornado: 2D Micro-XRF with ultimate speed and accuracy, (<https://www.bruker.com/products/x-ray-diffraction-and-elemental-analysis/micro-xrf-and-txrf/m4-tornado/overview.html>).
- Cavanagh, P.D., and Bish, D.L., 2016, Linear programming approach to quantitative mineralogy on Mars: Lunar and Planetary Science Conference, 47th, Woodlands, Texas, Proceedings, p. 1–2.
- Cheary, R.W., and Coelho, A., 1992, A fundamental parameters approach to X-ray line-profile fitting: *Journal of Applied Crystallography*, v. 25, p. 109–121.
- Cline, J.S., 2018, Nevada's Carlin-type gold deposits: What we've learned during the past 10 to 15 years: *Reviews in Economic Geology*, v. 20, p. 7–37.
- Cline, J.S., Hofstra, A.H., Muntean, J.L., Tosdal, R.M., and Hickey, K.A., 2005, Carlin-type gold deposits in Nevada: Critical geologic characteristics and viable models: *Economic Geology 100th Anniversary Volume*, p. 451–484.
- Croudace, I.W., and Rothwell, R.G., 2015, *Micro-XRF studies of sediment cores: Applications of a non-destructive tool for the environmental sciences*: Dordrecht, New York, Springer, 655 p.
- Elam, W., Ravel, B., and Sieber, J., 2002, A new atomic database for X-ray spectroscopic calculations: *Radiation Physics and Chemistry*, v. 63, p. 121–128.
- Elam, W., Shen, R., Scruggs, B., and Nicolosi, J., 2004, Accuracy of standardless FP analysis of bulk and thin film samples using a new atomic database: *Advances in X-Ray Analysis*, v. 47, p. 104–109.
- Emsbo, P., Hofstra, A.H., Lauha, E.A., Griffin, G.L., and Hutchinson, R.W., 2003, Origin of high-grade gold ore, source of ore fluid components, and genesis of the Meikle and neighboring Carlin-type deposits, northern Carlin Trend, Nevada: *Economic Geology*, v. 98, p. 1069–1105.
- Flude, S., Haschke, M., and Storey, M., 2017, Application of benchtop micro-XRF to geological materials: *Mineralogical Magazine*, v. 81, p. 923–948.
- Fox, D.C.M., Spinks, S.C., Pearce, M.A., Barham, M., Le Vaillant, M., Thorne, R.L., Aspandiar, M., and Verrall, M., 2019, Plundering Carlow Castle: First look at a unique Mesoarchean-hosted Cu-Co-Au deposit: *Economic Geology*, v. 114, p. 1021–1031.
- Genna, D., Gaboury, D., Moore, L., and Mueller, W.U., 2011, Use of micro-XRF chemical analysis for mapping volcanogenic massive sulfide related hydrothermal alteration: Application to the subaqueous felsic dome-flow complex of the Cap d'Ours section, Glenwood rhyolite, Rouyn-Noranda, Québec, Canada: *Journal of Geochemical Exploration*, v. 108, p. 131–142.
- Gottlieb, P., 2008, The revolutionary impact of automated mineralogy on mining and mineral processing: *International Mineral Processing Congress, 24th*, Beijing, China, September 2008, Proceedings, p. 165–174.
- Hill, R.J., and Howard, C.J., 1987, Quantitative phase-analysis from neutron powder diffraction data using the Rietveld method: *Journal of Applied Crystallography*, v. 20, p. 467–474.
- Johnson, C.L., Browning, D.A., and Pendock, N.E., 2019, Hyperspectral imaging applications to geomaterials: Utilizing blast hole mineralogy to predict Au-Cu recovery and throughput at the Phoenix mine, Nevada: *Economic Geology*, v. 114, p. 1481–1494.
- Kanngießner, B., 2003, Quantification procedures in micro X-ray fluorescence analysis: *Spectrochimica Acta Part B: Atomic Spectroscopy*, v. 58, p. 609–614.
- Mervine, E.M., Wilson, S.A., Power, I.M., Dipple, G.M., Turvey, C.C., Hamilton, J.L., Vanderzee, S., Raudsepp, M., Southam, C., Matter, J.M., Kelemen, P.B., Stiefenhofer, J., Miya, Z., and Southam, G., 2018, Potential for offsetting diamond mine carbon emissions through mineral carbonation of processed kimberlite: An assessment of De Beers mine sites in South Africa and Canada: *Mineralogy and Petrology*, v. 112, p. 755–765.
- Muntean, J.L., 2018, The Carlin gold system: Applications to exploration in Nevada and beyond: *Reviews in Economic Geology*, v. 20, p. 1–6.
- R Core Team, 2017, R: A language and environment for statistical computing: Vienna, Austria, R Foundation for Statistical Computing, v. 3.5.2.
- Rietveld, H.M., 1969, A profile refinement method for nuclear and magnetic structures: *Journal of Applied Crystallography*, v. 2, p. 65–71.
- Ryan, C.G., Kirkham, R., Moorhead, G.F., Parry, D., Jensen, M., Faulks, A., Hogan, S., Dunn, P.A., Dodanwala, R., Fisher, L.A., Pearce, M., Siddons, D.P., Kuczewski, A., Lundström, U., Trolliet, A., and Gao, N., 2018, Maia Mapper: High definition XRF imaging in the lab: *Journal of Instrumentation*, v. 13, no. 03, p. C03020–C03020.
- Scarlett, N.V.Y., and Madsen, I.C., 2006, Quantification of phases with partial or no known crystal structures: *Powder Diffraction*, v. 21, no. 4, p. 278–284.
- Sherman, J., 1955, The theoretical derivation of fluorescent X-ray intensities from mixtures: *Spectrochimica Acta*, v. 7, p. 283–306.
- Smith, R.J., 2009, Use and misuse of the reduced major axis for line-fitting: *American Journal of Physical Anthropology*, v. 140, p. 476–486.
- Steiner, A.P., and Hickey, K.A., 2019, Ore-stage calcite veins in the Carlin-type Au-deposits of the Nadaleen trend, Yukon: A new addition to the economic geologist's tool-kit: *Society for Geology Applied to Mineral Deposits (SGA) Biennial Meeting, 15th*, Glasgow, Scotland, Proceedings, v. 1, p. 267–270.
- Stephens, P.W., 1999, Phenomenological model of anisotropic peak broadening in powder diffraction: *Journal of Applied Crystallography*, v. 32, p. 281–289.
- Stewart, J.H., 1980, *Geology of Nevada: A discussion to accompany the Geologic Map of Nevada*, Reno: Nevada Bureau of Mines and Geology, *Geologic Map of Nevada, Special Publication 4*, 136 p.
- Tagle, R., and Reinhardt, F., 2016, Standardless and standard-supported fundamental parameter quantification of steel samples: Bruker Lab Report XRF 465, 4 p. (https://www.bruker.com/fileadmin/user_upload/8-PDF-Docs/X-rayDiffraction_ElementalAnalysis/mXRF/LabReports/LR_m4_tornado_xrf_465_steel_quantification_lores.pdf)
- Thomsen, V., 2007, Basic fundamental parameters in X-ray fluorescence: *Spectroscopy*, v. 22, no. 5, p. 46–50.
- Turvey, C.C., Hamilton, J.L., and Wilson, S.A., 2018, Comparison of Rietveld-compatible structureless fitting analysis methods for accurate quantification of carbon dioxide fixation in ultramafic mine tailings: *American Mineralogist*, v. 103, p. 1649–1662.
- Vaughan, J.R., Hickey, K.A., and Barker, S.L.L., 2016, Isotopic, chemical, and textural evidence for pervasive calcite dissolution and precipitation accompanying hydrothermal fluid flow in low-temperature, carbonate-hosted, gold systems: *Economic Geology*, v. 111, p. 1127–1157.
- Węgrzynek, D., Hołyńska, B., and Ostachowicz, B., 1998, A comparison of the performance of a fundamental parameter method for analysis of total reflection X-ray fluorescence spectra and determination of trace elements,

- versus an empirical quantification procedure: *Spectrochimica Acta Part B: Atomic Spectroscopy*, v. 53, no. 1, p. 43–48.
- Willis, J.P., Turner, K., and Pritchard, G., 2011, XRF in the workplace: A guide to practical XRF spectrometry: Chipping Norton, N.S.W, PANalytical Australia, 252 p.
- Wilson, S.A., Raudsepp, M., and Dipple, G.M., 2006, Verifying and quantifying carbon fixation in minerals from serpentine-rich mine tailings using the Rietveld method with X-ray powder diffraction data: *American Mineralogist*, v. 91, p. 1331–1341.
- 2009, Quantifying carbon fixation in trace minerals from processed kimberlite: A comparative study of quantitative methods using X-ray powder diffraction data with applications to the Diavik diamond mine, Northwest Territories, Canada: *Applied Geochemistry*, v. 24, p. 2312–2331.
- Xu, J., Zhu, S.-Y., Luo, T.-Y., Zhou, W., and Li, Y.-L., 2015, Uranium mineralization and its radioactive decay-induced carbonization in a black shale-hosted polymetallic sulfide ore layer, Southwest China: *Economic Geology*, v. 110, p. 1643–1652.



Rocky Barker obtained his M.Sc. degree in geoscience from Colorado State University in 2017. He has worked as a geoscientist and data science consultant in the mineral industry for companies such as Barrick Gold Exploration Inc., Nevada Gold Mines, and AusSpec. He is currently a third-year Ph.D. candidate at the University of Waikato in Hamilton, New Zealand. Rocky's Ph.D. work focuses on the prediction of mineralogy and mineral chemistry in a Carlin-type gold deposit using hyperspectral infrared data. His study involves the integration of geochemical datasets collected at various scales, supported by machine learning methods.

